Momentum distributions in stripping reactions of radioactive projectiles at intermediate energies

C. A. Bertulani[1] and P. G. Hansen[1,2]

[1]*Department of Physics and Astronomy, Michigan State University, East Lansing, Michigan 48824*

[2]*National Superconducting Cyclotron Laboratory, Michigan State University, East Lansing, Michigan 48824**

(Dated: July 7, 2004)

Abstract

The theory of one-nucleon removal in the stripping reaction (inelastic breakup) on a light target is extended to cover two-dimensional momentum distributions of the reaction residues with the use of realistic profile functions for the core-target and nucleon-target interactions. Examples of the calculated projected parallel- and transverse momentum distributions are given. The transverse momentum distributions, projections on a Cartesian axis perpendicular to the beam direction, show an interesting intermingling of the stripping reaction with elastic scattering of the reaction residue on the target. We also obtain doubly-differential distributions of the cross section on the parallel- and transverse-momentum variables. The distributions depend strongly on the value of the magnetic quantum number m. They will be of importance for evaluating acceptance corrections in experiments, and they lead to alignment with the possibility of anisotropic emission of subsequent gamma rays, an interesting spectroscopic tool. Experimental data for proton stripping of ^{8}B agree with our calculations.

PACS numbers: 21.10.Jx,24.50.+g, 25.60.-t, 27.20.+n

Keywords: Knockout reactions, eikonal theory, parallel- and transverse-momentum distributions

*Electronic address: hansen@nscl.msu.edu

I. INTRODUCTION

Single-nucleon knockout reactions with heavy ions, at intermediate energies and in inverse kinematics, have become a specific and quantitative tool for studying single-particle occupancies and correlation effects in the nuclear shell model, see the recent review [1]. The high sensitivity of the method has allowed measurements on rare radioactive species available in intensities of less than one atom per second for the incident beam. The experiments observe reactions in which fast, mass A, projectiles with laboratory momentum $\mathbf{k}_A = \mathbf{P}_A/\hbar$ collide peripherally with a light nuclear target, typically ^{9}Be, producing residues with mass $(A-1)$, in the following referred to as the core (c) of the assumed two-body system of core plus nucleon. In the laboratory system the momentum transferred to the core is

$$\mathbf{k}_{c,lab} = \frac{A-1}{A}\mathbf{k}_A - \mathbf{k}_{A-1}. \tag{1}$$

The final state of the target and that of the struck nucleon are not observed, but instead the energy of the final state of the residue can be identified by measuring coincidences with decay gamma-rays emitted in flight. Referred to the center-of-mass system of the projectile, the transferred momentum is $\mathbf{k}_c$. In the sudden approximation and for the stripping reaction, defined below, this must equal the momentum of the struck nucleon before the collision. The measured partial cross sections to individual final levels provide spectroscopic factors for the individual angular-momentum components j. In complete analogy to the use of angular distributions in transfer reactions, the orbital angular momentum l is in the knockout reactions revealed by the differential cross section as a function of $\mathbf{k}_c$. These distributions are the subject of the present paper.

The early interest in momentum distributions came from studies of nuclear halo states, for which the narrow momentum distributions, in a qualitative way, revealed the large spatial extension of the halo wave function. It was pointed out by Bertulani and McVoy [2] that the longitudinal component of the momentum (taken along the beam or z direction) gives the most accurate information on the intrinsic properties of the halo and that it is insensitive to details of the collision and the size of the target. In contrast to this, the transverse distributions of the core are significantly broadened by diffractive effects and by Coulomb scattering. For experiments that observe the nucleon produced in elastic breakup, the transverse momentum is entirely dominated by diffractive effects, as illustrated [3] by the angular distribution of the neutrons from the reaction ^{9}Be(^{11}Be,^{10}Be+n)X. In this case, the width of the transverse momentum distribution reflects essentially the size of the target. Experiments and theory for reactions of neutron halos have bee reviewed in ref. [4]. It was found that to understand the measured longitudinal momentum distributions it is necessary to take into account that a heavy-ion knockout reaction, being surface-dominated, can only sample the external part of the nucleon wave function. The magnitude of the reaction cross section is determined by the part of the wave function that is accessed, and the shape of the momentum distribution reflects the momentum content in this part. Calculations [4, 5, 6] based on a sharp-surface strong-absorption ("black-disk") model could account for the observed longitudinal momentum distributions and also, approximately, for the absolute cross sections. This approach is confirmed in the, more accurate, present work, which extends the theory to include the general dependence of the differential cross section on the momentum vector.

It is essential to note that the cross section for the production of a given final state of the residue has two contributions. The most important of the two, commonly referred

to as stripping or inelastic breakup, represents all events in which the removed nucleon reacts with and excites the target from its ground state. The second component, called diffractive or elastic breakup, represents the dissociation of the nucleon from the residue through their two-body interactions with the target, each being at most elastically scattered. These events result in the ejected nucleon being present in the forward beam with essentially beam velocity, and the target remaining in its ground state. These processes lead to different final states, they are incoherent, and their cross sections must be added in measurements where only the residue is observed. General expressions for the total and differential cross sections for the two components have been given by Hencken, Bertsch and Esbensen [7].

In a subsequent development, the knockout method was extended to non-halo states [8, 9, 10, 11, 12, 13, 14]. For these, involving more deeply-bound nucleons, the one-nucleon stripping cross sections are much smaller than the free-nucleon reaction cross section on the same target; a ratio that gives a measure of how much the nucleon wave function is "shielded" from the target by the bulk of the core. This required a more elaborate theoretical treatment based on the elastic S-matrices S_c and S_n [15, 16] of the core and nucleon. For a general review of applications of this technique see ref. [1], which shows that very accurate theoretical single-particle cross sections are obtained in this way. However, the longitudinal momentum distributions have continued being calculated in the black-disk approximation. This simplification has been permissible because the assumed sharp surface of the target generates only transverse momentum components, which are integrated out in the final result.

In the present paper we treat the three-dimensional momentum distribution of the core in stripping reactions at the same level of approximation as the single-particle cross sections in Tostevin's calculations [9, 10]. Using S-matrices from this work, we obtain identical single-particle cross sections after integration over momentum and summation over the m_l substates. The results (i) test the reliability of the previously used sharp-surface approximation, and (ii) demonstrate that the transverse momentum distributions are quantitatively and even qualitatively different from the parallel momentum distributions, and (iii) can serve to extract angular-momentum information from the angular distributions of the residues. Finally, (iv) the results are of importance for calculating acceptance corrections in experiments, and we evaluate the correlations between longitudinal and transverse components. After a presentation of the main features of the theoretical calculations, we give examples of the distributions obtained for different values of the nucleon separation energy S_n and the orbital angular momentum l. Some essential numerical details are presented in an appendix.

II. CALCULATION OF THE DIFFERENTIAL STRIPPING CROSS SECTION

In this section we summarize the equations used in the calculation of stripping cross sections. The numerical calculations were done by using a Gaussian expansion method which is described in the appendix. We also show the equations used for the elastic scattering cross section, which will be important to interpret the numerical results obtained for the stripping cross sections, discussed in section 3.

Following ref. [7], the cross section for the stripping reaction $(c+n)+A \longrightarrow c+X$, where c corresponds to a specified final state of the core, is given by

$$\frac{d\sigma_{\rm str}}{d^3k_c} = \frac{1}{(2\pi)^3}\frac{1}{2l+1}\sum_m \int d^2b_n \left[1-\left|S_n\left(b_n\right)\right|^2\right]\left|\int d^3r\; e^{-i\mathbf{k}_c\cdot\mathbf{r}} S_c\left(b_c\right)\psi_{lm}\left(\mathbf{r}\right)\right|^2, \qquad (2)$$

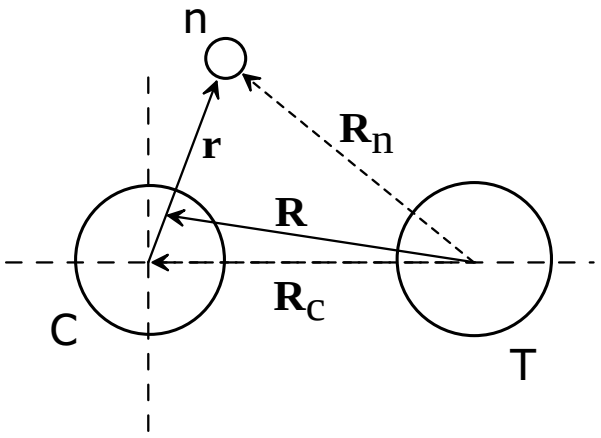

FIG. 1: Coordinates used in text.

and where $\mathbf{r} \equiv (\boldsymbol{\rho}, z, \phi) = \mathbf{R}_n - \mathbf{R}_c$, so that

$$\begin{aligned} b_c &= |\boldsymbol{\rho} - \mathbf{b}_n| = \sqrt{\rho^2 + b_n^2 - 2\rho\ b_n \cos(\phi - \phi_n)} \\ &= \sqrt{r^2 \sin^2\theta + b_n^2 - 2r \sin\theta\ b_n \cos(\phi - \phi_n)}\,. \end{aligned} \tag{3}$$

with the symbols $\mathbf{b}_c$ and $\mathbf{b}_n$ denoting two-dimensional vectors (see figure 1). S_c (S_n) are the S-matrices for the core+target and the neutron (or proton)+target scattering.

The single-particle bound state wave functions for the subsystem $(c+n)$, i.e. $\psi_{lm}(\mathbf{r})$, in eq. (2) are specified by $\psi_{lm}(\mathbf{r}) = R_l(r)\, Y_{lm}(\hat{\mathbf{r}})$, where $R_l(r)$ is the radial wave function. It is not necessary to specify the total single-particle angular momentum j, since the assumed interaction is spin-independent, and the depth of the single-particle potential well is adjusted to reproduce the effective nucleon binding energy.

The cross sections for the longitudinal momentum distributions are obtained by integrating eq. (2) over the transverse component of $\mathbf{k}_c$, i.e. over $\mathbf{k}_c^{\perp}$, and using

$$\int d^2\mathbf{k}_c^{\perp}\ \exp\left[-i\mathbf{k}_c^{\perp}.(\boldsymbol{\rho} - \boldsymbol{\rho}')\right] = (2\pi)^2\, \delta(\boldsymbol{\rho} - \boldsymbol{\rho}')\ . \tag{4}$$

One gets

$$\begin{aligned} \frac{d\sigma_{\rm str}}{dk_z} &= \frac{1}{2\pi}\frac{1}{2l+1}\sum_m \int d^2b_n\ \left[1 - |S_n(b_n)|^2\right]\ \int d^2\rho\ |S_c(b_n)|^2 \\ &\times\ \left|\int_{-\infty}^{\infty} dz\ \exp\left[-ik_z z\right]\psi_{lm}(\mathbf{r})\right|^2\ , \end{aligned} \tag{5}$$

where k_z represents the longitudinal component of $\mathbf{k}_c$.

For the transverse momentum distribution in cylindrical coordinates $k_\perp = \sqrt{k_x^2 + k_y^2}$, one uses in eq. (2)

$$\int_{-\infty}^{\infty} dk_z\ \exp\left[-ik_z(z - z')\right] = 2\pi\delta(z - z')\ , \tag{6}$$

and the result is

$$\frac{d\sigma_{\rm str}}{d^2k_\perp} = \frac{1}{2\pi}\frac{1}{2l+1}\int d^2b_n \left[1-\left|S_n\left(b_n\right)\right|^2\right] \times \sum_{m,\ p}\int_{-\infty}^{\infty} dz \left|\int d^2\rho \ \exp\left(-i\mathbf{k}_c^{\perp}.\boldsymbol{\rho}\right) S_c\left(b_n\right)\psi_{lm}\left(\mathbf{r}\right)\right|^2 . \tag{7}$$

Sometimes it is convenient to describe the transverse momentum distributions in terms of the projection onto one of the Cartesian components of the transverse momentum. This can be obtained directly from eq. (7), i.e.

$$\frac{d\sigma_{\rm str}}{dk_y} = \int dk_x \ \frac{d\sigma_{\rm str}}{d^2k_\perp}\left(k_x,k_y\right) \ . \tag{8}$$

The total stripping cross section can be obtained by integrating either eq. (5) or eq. (7). For example, from eq. (5), using eq. (6), one obtains

$$\sigma_{\rm str} = \frac{2\pi}{2l+1}\int_0^{\infty} db_n \ b_n \ \left[1-\left|S_n\left(b_n\right)\right|^2\right] \times \int d^3r \ \left|S_c\left(\sqrt{r^2\sin^2\theta+b_n^2-2r\sin\theta \ b_n\cos\phi}\right)\right|^2 \ \sum_m \left|\psi_{lm}\left(\mathbf{r}\right)\right|^2 \ , \tag{9}$$

which is the same as eq. (12) of ref. [7].

In the appendix A we show how the integrals in eqs. (5) and (7) can be evaluated numerically with use of Gaussian expansions of the core/nucleon+target S-matrices.

The S-matrices have been obtained using the eikonal approximation for the wave functions. In this approximation the outgoing wave of a fragment, with wave number $\mathbf{k}$, is given by

$$\left\langle \mathbf{r}|\Psi_{\mathbf{k}}^{(+)}\right\rangle = \exp\left\{i\mathbf{k}\cdot\mathbf{r}+\frac{i}{\hbar v}\int_z^{\infty} dz' U_{opt}(r')\right\} \ . \tag{10}$$

The overlap of the incoming and outgoing wave function becomes

$$\left\langle \Psi_{\mathbf{k}}^{(-)}|\Psi_{\mathbf{k}'}^{(+)}\right\rangle = S\left(b\right)\exp\left(i\mathbf{q}.\mathbf{r}\right) \ , \tag{11}$$

where $\mathbf{q}=\mathbf{k}'-\mathbf{k}$ is the momentum transfer and $S\left(b\right)$ is the scattering matrix given by

$$S\left(b\right)=\exp\left[i\chi(b)\right], \qquad \text{with} \qquad \chi(b)=-\frac{1}{\hbar v}\int_{-\infty}^{\infty} dz \ U_{opt}(r) \ , \tag{12}$$

and $U_{opt}(\mathbf{r})$ is the appropriate optical potential for the core+target and the neutron (or proton)+target scattering. In equation (12) $\chi(b)$ is the eikonal phase, and $r=\sqrt{b^2+z^2}$, where b is often interpreted as the impact parameter. This interpretation arises from a comparison of the results obtained with eikonal wavefunctions with those obtained with classical particles colliding at a given impact parameter b [17]. Nonetheless, the eikonal wavefunction is a quantum scattering state and b is the transverse coordinate associated to it. Thus wave-mechanical effects, like smearing and interference, are accounted for properly.

In the optical limit of the Glauber theory, the eikonal phase is obtained from the nuclear ground state densities and the nucleon-nucleon cross sections by the relation [17]

$$\chi(b)=\int_0^{\infty} dq \ q \ \rho_p\left(q\right)\rho_t\left(q\right)f_{NN}\left(q\right)J_0\left(qb\right) \ , \tag{13}$$

where J_0 is the Bessel function of order zero, $\rho_{p,t}(q)$ is the Fourier transform of the nuclear densities of the projectile and target, and $f_{NN}(q)$ is the high-energy nucleon-nucleon scattering amplitude at forward angles, which can be parametrized by [18]

$$f_{NN}(q) = \frac{k_{NN}}{4\pi}\sigma_{NN}(i+\alpha_{NN})\exp\left(-\beta_{NN}q^2\right) \ . \tag{14}$$

In this equation σ_{NN}, α_{NN}, and β_{NN} are parameters which fit the high-energy nucleon-nucleon scattering at forward angles. In eq. (13) the quantities $\rho_p(q)$ and $\rho_t(q)$ are calculated from the radial density distributions, usually [1] taken to be of Gaussian shapes for light nuclei, and of Fermi shapes for heavier nuclei with parameters taken from experiment. For cases where more accuracy is needed, it is possible to take the density distributions and the nucleon-core bound-state wave function from Hartree-Fock calculations, as has been done in some recent work. This demonstrates that the theoretical uncertainty on the integral single-particle cross section (*i.e.* for a spectroscopic factor of unity) is of the order of 5% for a halo state [19] and 15% for a very deeply bound $l = 2$ state ($S_n = 22$ MeV) [20]. The precise choice of input parameters influences the absolute spectroscopic factors, which have been the subject of many previous papers [1, 8, 11, 12, 13, 14, 19, 20] to which we refer for numerical details. However, it means little for the shapes of the momentum distributions which are the focus of the present work, and it will not be discussed further here.

For the Coulomb part of the optical potential the integral in eq. (12) diverges. One solves this by using $\chi = \chi_N + \chi_C$, where χ_N is given by eq. (12) without the Coulomb potential and writing the Coulomb eikonal phase, χ_C as

$$\chi_C(b) = 2\eta\ln(kb) \ , \tag{15}$$

where $\eta = Z_pZ_te^2/\hbar v$, Z_p and Z_t are the charges of projectile and target, respectively, v is their relative velocity, k their wavenumber in the center of mass system. Eq. (15) reproduces the exact Coulomb scattering amplitude when used in the calculation of the elastic scattering with the eikonal approximation [17]:

$$f_C(\theta) = \frac{Z_pZ_te^2}{2\mu v^2\ \sin^2(\theta/2)}\ \exp\left\{-i\eta\ \ln\left[\sin^2(\theta/2)\right] + i\pi + 2i\phi_0\right\} \tag{16}$$

where $\phi_0 = arg\Gamma(1+i\eta/2)$. This is convenient for the numerical calculations since, as shown below, the elastic scattering amplitude can be written with the separate contribution of the Coulomb scattering amplitude included. Then, the remaining integral (the second term on the r.h.s. of eq. (21) below) converges rapidly for the scattering at forward angles.

Although the Coulomb phase in eq. (15) diverges at $b = 0$, this does not pose a real problem, since the strong absorption suppresses the scattering at small impact parameters. It is also easy to correct this expression to account for the finite charge distribution of the nucleus. For example, assuming a uniform charge distribution with radius R the Coulomb phase becomes

$$\begin{aligned}\chi_C(b)\ = 2\eta\ \Big\{&\Theta(b-R)\ \ln(kb) + \Theta(R-b)\left[\ln(kR) + \ln(1+\sqrt{1-b^2/R^2})\right.\\ &\left.-\sqrt{1-b^2/R^2} - \tfrac{1}{3}(1-b^2/R^2)^{3/2}\right]\Big\}\ ,\end{aligned} \tag{17}$$

where Θ is the step function. This expression is finite for $b = 0$, contrary to eq. (15). If one assumes a Gaussian distribution of charge with radius R, appropriate for light nuclei, the

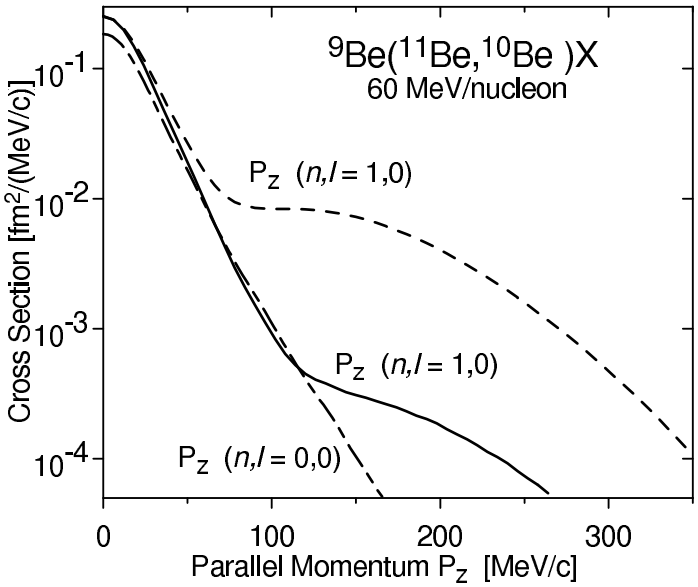

FIG. 2: Longitudinal momentum distribution for the residue in the ^{9}Be(^{11}Be,^{10}Be$_{gs}$)X reaction at 60 MeV/nucleon as studied in the experiment of Aumann *et* al. [12]. The dashed curve is the cross section calculated in the transparent limit, re-scaled by a factor of 0.535. It has a high-energy component arising from the inner lobe of the wave function. The full drawn curve is the result of the present work. The black disk calculation (not shown) is essentially indistinguishable from this, except for the high-momentum tail. The dot-dashed curve shows that the weak shoulder is not present with an assumed nodeless 0*s* wave function with the same binding energy (0.504 keV).

Coulomb phase becomes

$$\chi_C(b) = 2\eta \ \left[\ln(kb) + \frac{1}{2}E_1(b^2/R^2)\right] \ , \tag{18}$$

where the error function E_1 is defined as

$$E_1(x) = \int_x^\infty \frac{e^{-t}}{t}\ dt \ . \tag{19}$$

This phase also converges as $b \to 0$. In eq. (17) $R = R_p + R_t$, while in eq. (18) $R = \sqrt{R_p^2 + R_t^2}$, where R_p and R_t are the respective projectile and target radius. The cost of using the expressions (17) and (18) is that the Coulomb scattering amplitude becomes more complicated than (16). Moreover, we have numerically attested that the elastic and inelastic scattering cross sections change very little by using eqs. (17) or (18), instead of eq. (15).

In calculations involving stripping, the final state Coulomb interaction between the core and the target is taken into account by using the eikonal-Coulomb phase shift of (15) in the calculation of S_c. However in the calculation of diffraction dissociation both S_c and S_n are calculated using the eikonal-Coulomb phase shift of (15).

The calculation of elastic scattering amplitudes using eikonal wave functions, eq. (10), is very simple. They are given by [17]

$$f_{el}(\theta) = ik \ \int_0^\infty db\ b\ J_0(qb)\ \ \{1 - \exp\left[i\chi(b)\right]\} \ , \tag{20}$$

where $q = 2k\sin(\theta/2)$, and θ is the scattering angle. The elastic scattering cross section is $d\sigma_{el}/d\Omega = |f_{el}(\theta)|^2$. For numerical purposes, it is convenient to make use of the analytical formula, eq. (16), for the Coulomb scattering amplitude. Thus, if one adds and subtracts the Coulomb amplitude, $f_C(\theta)$ in eq. (20), one gets

$$f_{el}(\theta) = f_C(\theta) + ik \int_0^\infty db\ b\ J_0(qb)\ \exp\left[i\chi_C(b)\right]\ \{1 - \exp\left[i\chi_N(b)\right]\}\ . \tag{21}$$

The advantage of using this formula is that the term $1 - \exp\left[i\chi_N(b)\right]$ becomes zero for impact parameters larger than the sum of the nuclear radii (grazing impact parameter). Thus, the integral needs to be performed only within a small range. In this formula, χ_C is given by eq. (15) and $f_C(\theta)$ is given by eq. (16), with

$$\phi_0 = -\eta C + \sum_{j=0}^{\infty}\left(\frac{\eta}{j+1} - \arctan\frac{\eta}{j+1}\right)\ , \tag{22}$$

where $C = 0.5772156...$ is Euler's constant.

The elastic cross section can be expressed in terms of the transverse momentum by using the relationships $d\Omega \simeq d^2k_\perp/k^2$, and $k_\perp \simeq q = 2k\sin(\theta/2)$, valid for high-energy collisions.

III. EXAMPLES OF MOMENTUM DISTRIBUTIONS

We explore the consequences of the expressions developed in sect. II by calculating momentum distributions for selected cases. The longitudinal momentum distributions, corresponding to a projection on the beam (P_z) axis, turn out to be very close to those obtained in the simpler black-disk approximation [4, 5, 6]. For this reason, a comparison with the numerous experimental data available is hardly necessary, but some references are given. A general discussion of longitudinal momentum distributions can be found in [1]. For the distribution projected to an axis perpendicular to the beam axis, the situation is different. We find in all cases an interesting intermingling of momentum components arising from stripping of the nucleon and from elastic scattering of the core fragment on the target. The latter mechanism is diffractive for light targets and Coulomb-dominated for heavy targets. There is very little useful experimental evidence on the transverse momentum distributions, as only the observation of coincident gamma rays can separate out the differential cross sections to individual final levels. (Even for halo nuclei, such as ^{11}Be and ^{15}C, 20–30% of the inclusive cross section goes to excited levels with different l values.)

We have chosen to represent the momentum distributions graphically in the following way. Projections onto a single Cartesian coordinate are shown for one half axis only (the P_z distribution is symmetric in the eikonal approximation). For cases where the magnetic quantum number m differs from zero, we have weighted the differential cross section with the multiplicity of 2, so that the sum over all m components gives the total cross section. The two-dimensional momentum distribution does not depend on the azimuthal angle. It is convenient to present it as a function of the parallel and the transverse momentum with the definition

$$\frac{d^2\sigma_{\rm str}}{dk_\perp dk_z} = 2\pi k_\perp \frac{d^3\sigma_{\rm str}}{d^2k_\perp dk_z}, \tag{23}$$

which normalizes to the total cross section when the integration is extended over the negative k_z axis.

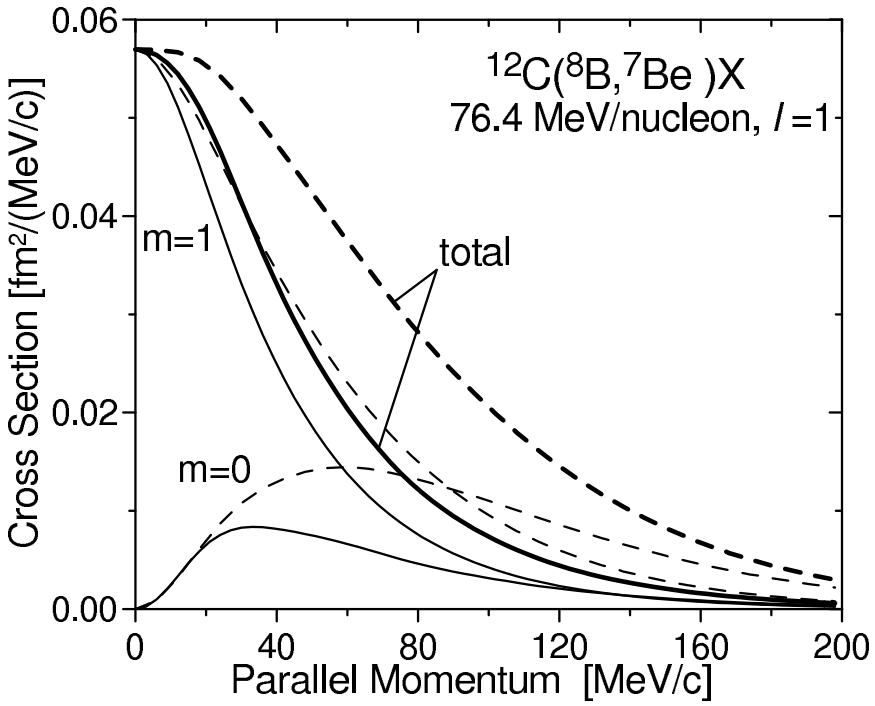

FIG. 3: Longitudinal momentum distribution for the residue in the ^{12}C(^{8}B,^{7}Be$_{gs}$)X reaction at 76 MeV/nucleon as studied in the experiment of Enders *et* al. [14]. The proton binding energy for this proton halo state is 0.137 MeV. The dashed curves are the cross sections calculated in the transparent limit, re-scaled by a factor of 0.35. The narrower full drawn curves are the results of the present work. The thin curves show individual $m = \pm 1$ components with the sums given as thick lines. The black disk calculation (not shown) gives very similar results. Fig. 4 of ref. [1] compares a similar (black-disk) calculation with experimental data.

A. Longitudinal momentum distributions

The deuteron was the first halo system to be studied. Serber [21] calculated the momentum spectrum of neutrons from deuteron breakup on a light target in an approximation that amounts to replacing the core S-matrix $S_c\,(b_c)$ in eq. (2) by unity. This leads to the expression

$$\frac{d\sigma_{\rm str}}{d^3k_c} = \frac{1}{(2\pi)^3}\frac{1}{2l+1}\;\sigma_{pT}\sum_m \left|\int d^3r\; e^{-i\mathbf{k}_c\cdot\mathbf{r}}\psi_{lm}\,(\mathbf{r})\right|^2, \tag{24}$$

where σ_{pT} is the proton-target reaction cross section, so that the stripping cross section (the term coined by Serber, see his comment in [22]) is that of a free proton, and the momentum distribution is the Fourier transform of the bound-state wave function. This is an excellent approximation for the deuteron, and it served later to explain qualitatively why early studies of stripping reactions of halo nuclei observed narrow transverse and longitudinal momentum distributions [23, 24].

However, the transparent-core limit is never a good approximation for reactions of nuclei heavier than the deuteron. It overestimates the stripping cross section by a factor 2 for a pronounced halo system such as ^{11}Be, and by up to a factor of 25 for deeply bound nucleons. The momentum distributions are also modified in a significant way by the absorption given by the core S-matrix $S_c\,(b_c)$ as shown by the examples of the $l = 0$ ^{11}Be neutron halo and

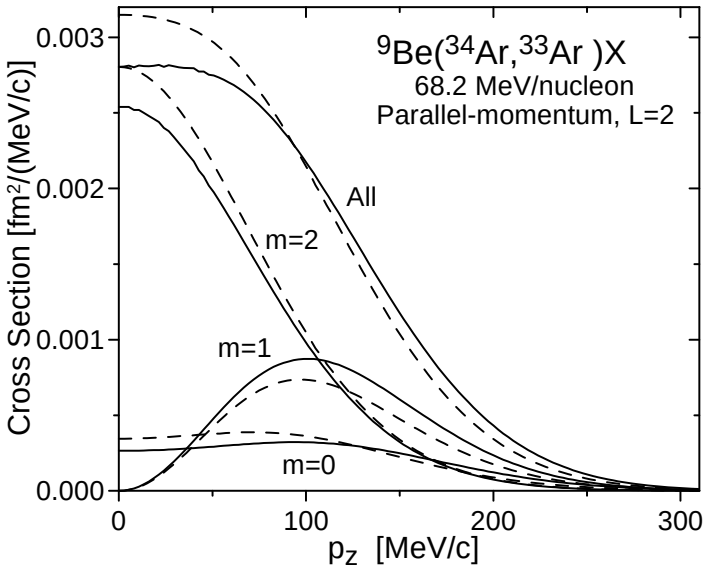

FIG. 4: Longitudinal momentum distributions for the reaction ^{9}Be(^{34}Ar,^{33}Ar($\frac{3}{2}^+$)) at 68.2 MeV/nucleon. This $l = 2$ neutron-removal reaction leads to a final $\frac{3}{2}^+$ level bound by 18.42 MeV. The solid curves represent the exact calculations and the dashed curves the sharp-cutoff approximation.

the $l = 1$ ^{8}B proton halo shown in figs. 2 and 3. The underlying reason is that the knockout reaction of a heavy ion on an absorptive target, such as ^{9}Be, is surface dominated and samples only the momentum components there and in the tail of the wave function. The case of ^{11}Be in fig. 2 is good demonstration of this: The high-momentum components (the "shoulder") seen in the $S_c\,(b_c) = 1$ approximation arise from the inner lobe in the wave function of the second s state and vanish almost completely in the knockout reaction, which cannot "see" the interior of the projectile.

In the case of the $l = 1$ knockout on ^{8}B, shown in fig. 3, both m components are much narrower than in the transparent-core approximation, and the $m = 0$ state is suppressed relative to the $m = \pm 1$ states. A simple geometrical argument [6] accounts for this: Projected onto the (x, y) plane, the two lobes of $m = 0$ wave function are oriented along the z axis and shielded by the core from interacting (alone) with the target.

The sharp-cutoff model [3, 5, 6] has been a useful tool for discussing parallel-momentum distributions. In this approximation the S-matrices $S_c\,(b_c)$ and $S_n\,(b_n)$ (see fig. 1) are replaced by step functions with radii chosen to approximate the free core-target and nucleon-target cross sections by means of two parameters, a target radius and a minimum-impact parameter. In the following we have scaled the latter by a factor of typically 0.95 to get agreement with the, more accurate, total cross sections. This adjustment has essentially no influence on the calculated shapes. For the two halo cases discussed in figs. 2 and 3 there is essentially no difference from the more exact calculation. The same is true for the deeply bound s state shown later, in fig. 7.

The case of a deeply bound state with $l = 2$ is shown in fig. 4. The reaction ^{9}Be(^{34}Ar,^{33}Ar($\frac{3}{2}^+$)) at 68.2 MeV/nucleon has a separation energy of 18.42 MeV and has been studied experimentally by Gade *et al.* [25]. The solid curves are exact calculations and the dashed curves are obtained with the sharp-cutoff approximation. In this case there is a

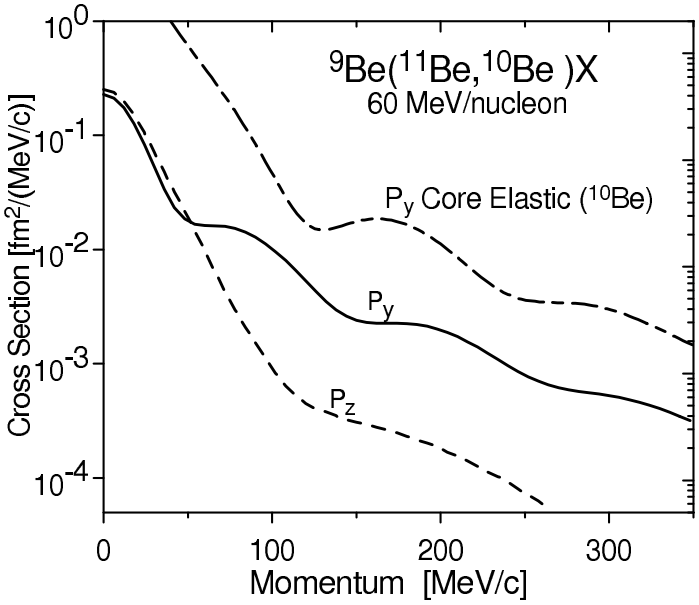

FIG. 5: Transverse momentum distribution (full drawn) for the reaction ^{9}Be (^{11}Be,^{10} Be$_{\rm gs}$) at 60 MeV/nucleon. The corresponding longitudinal momentum distribution (dashed) is shown for comparison. The dot-dashed curve is the calculated elastic cross section for the core.

noticeable difference.

Finally, we draw attention to an interesting effect that clearly is outside the scope of the present paper. The experiment on ^{34}Ar [25] shows an excess of intensity at the low-energy side of the $l = 0$ and $l = 2$ momentum distributions. This cannot be accounted for in the eikonal approximation as presented here, since it does not contain multistep time dependence, does not conserve energy, and yields symmetric line shapes. A similar low-momentum tail was observed in the $l = 0$ momentum distributions from neutron knockout on the ^{11}Be and ^{15}C halo states [26]. In this case, it was interpreted as arising from the diffractive reaction channel and could be quantitatively accounted for in a coupled-channels calculation. However, diffraction dissociation is a small contribution to the cross section in the case of ^{34}Ar and is hardly the explanation here. We have no explanation for this asymmetry, which has been seen also in other cases, and which remains an interesting problem for future investigations.

B. Transverse momentum distributions

Transverse momentum distributions depend more strongly on the details of the nucleus-nucleus interaction than do the longitudinal momentum distributions [2]. The nuclear size, the diffuseness of the nuclear matter distribution, and the core-target Coulomb repulsion all contribute to the transverse momentum distributions. At large impact parameters the Coulomb force still has a strong influence, especially for heavy targets, which for halo systems make Coulomb dissociation the dominant breakup channel.

In figure 5 we compare the longitudinal and transverse momentum distributions for the reaction ^{9}Be (^{11}Be,^{10} Be) at 60 MeV/nucleon. The transverse momentum distribution (solid

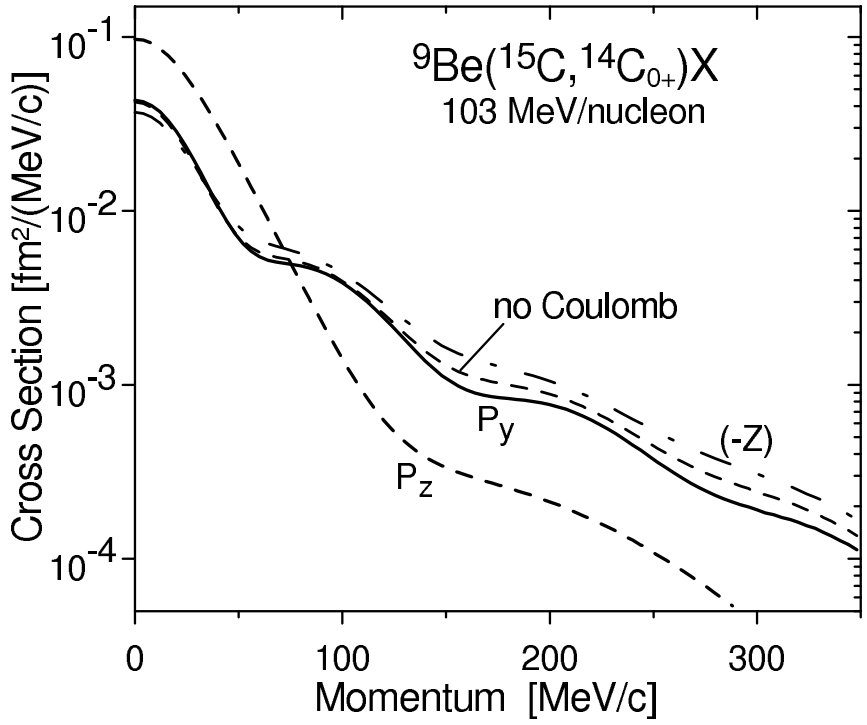

FIG. 6: Transverse momentum distribution (full drawn) for the reaction ^{9}Be (^{15}C,^{14} C$_{\rm gs}$) at 103 MeV/nucleon. The parallel-momentum distribution (dashed) has been studied experimentally [19, 26]. The influence of the Coulomb interaction is small, but visible with the log scale, for this target-core combination. The curves labelled "no Coulomb" and "(-Z)" represent a calculation with the target charge set to zero and to -4, respectively.

curve) has for small momenta the same shape as the longitudinal one (dashed), but is lower in intensity by about 10%. The missing cross section shows up as a broad distribution with an oscillatory pattern, which we interpret as elastic scattering of the core fragment simultaneously with the stripping of the neutron. We demonstrate this by calculating the core-target elastic cross section, which shows a similar pattern with the minima characteristic of Fraunhofer scattering. The minima are not in the same place, however, because of the condition that the neutron be absorbed in the stripping reaction. A similar broad component appears in the transverse momentum distribution of the core fragment in coupled-channels calculations of diffractive breakup (ref. [26] and J.A. Tostevin, personal communication).

For the case of ^{11}Be, bound by 0.504 MeV, the large size of the halo allows most absorption processes to occur without simultaneous elastic scattering of the core. For more bound states the two mechanisms become increasingly intermingled. Already in the stripping of the halo neutron of ^{15}C, bound by 1.218 MeV, the tail from core scattering is much stronger, as seen in fig. 6, and for the $l = 0$ neutron knockout from ^{34}Ar, bound by 17.06 MeV, the two mechanisms are no longer distinguishable, as seen in fig. 7. The case of knockout of a deeply bound $l = 2$ neutron, also from ^{34}Ar, is shown in fig. 8, which again shows a transverse momentum distribution that is broader than the longitudinal distribution shown in fig. 8. Note the different momentum dependence of the individual m components, which can easily be understood from geometrical properties of the spherical harmonics [6].

The longitudinal momentum distributions are not affected by elastic scattering of the

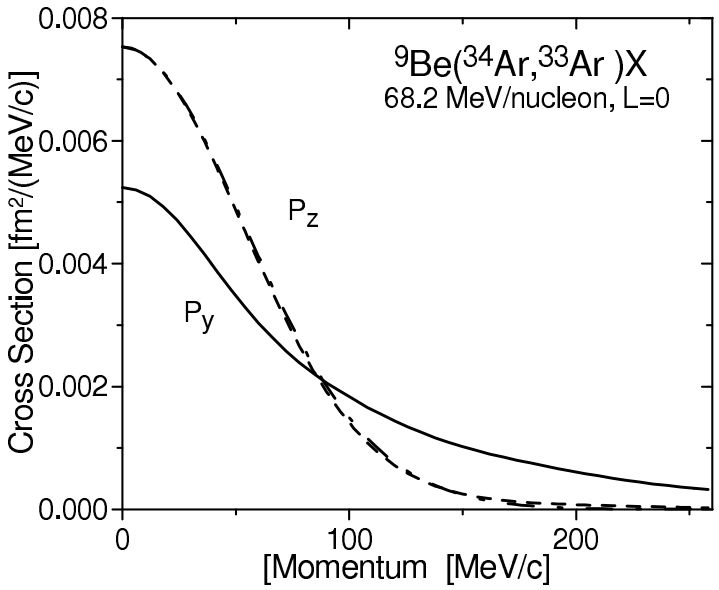

FIG. 7: Transverse momentum distribution (full drawn) for the $l = 0$ knockout reaction ^{9}Be(^{34}Ar,^{33} Ar($\frac{1}{2}^+$)) at 68 MeV/nucleon and with a neutron separation energy of 17.06 MeV [25]. The corresponding longitudinal momentum distribution (dashed) is essentially indistinguishable from the calculation in the black-disk approximation (dot-dashed).

core fragment. The basic reason for this is that the forces acting on the core fragment are along the z-direction and reverse sign at the origin of the z axis, thus leading to a null effect provided the angular deflection of the core fragment is small. For the same reason, the longitudinal momentum distributions are also relatively insensitive to Coulomb effects.

We now examine how the Coulomb force affects the transverse momentum distributions. In the case of a neutron halo, it pushes the core away from the target along the transverse direction. The resulting distributions for the case of a light target are here illustrated by carbon (Z=6) on beryllium (Z=4), shown in fig. 6. The effect is small and would hardly be measurable. We note, however, that leaving out the Coulomb interaction gives a broader momentum distribution, suggestive of an interference effect. There is an interesting way to explore this.

It is well known that the higher order Coulomb effects, e.g. to second-order in perturbation theory, carry information on the relative sign of the charge of the particles. In atomic physics this is often referred to as the Andersen-Barkas effect, which reflects contributions of odd powers in the projectile charge on stopping powers and ionization probabilities. In nuclear physics this idea has been explored in the study of dynamical effects in Coulomb dissociation [27]. We have carried out calculations reversing the sign of the target's charge but keeping all nuclear interactions constant. Fig. 6 shows that a hypothetical core-target Coulomb attraction, as could be expected, gives an even broader distribution. The reason for this is that the elastic scattering at large transverse momenta is dominated by the far-side scattering contribution, in which the nuclei pass by close to each other. For a negatively-charged target the nuclear and Coulomb forces interfere constructively, leading to larger deflection angles.

The Coulomb effect becomes important for heavier targets. To illustrate this, we compare

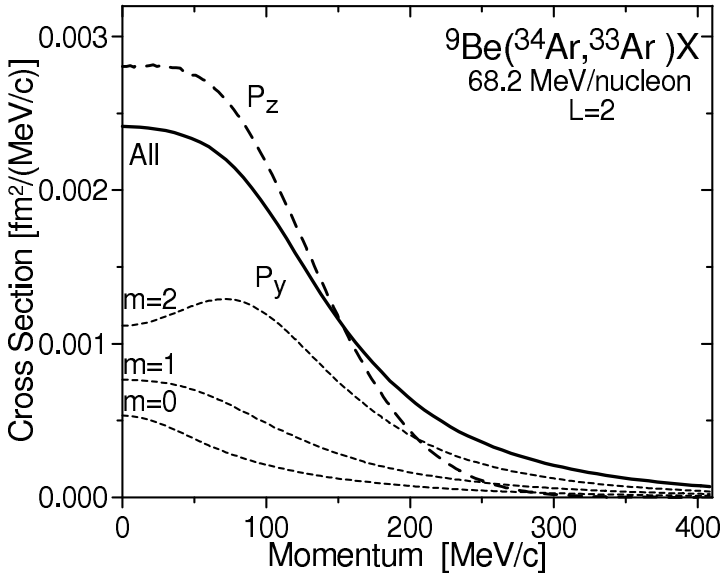

FIG. 8: Transverse momentum distribution (full drawn) for the $l = 2$ knockout reaction ^{9}Be (^{34}Ar,^{33} Ar) at 68 MeV/nucleon, corresponding to the $\frac{3}{2}^+$ excited level in the core with an effective neutron separation energy of 18.43 MeV. The longitudinal momentum distribution (dashed) is shown for comparison.

in figure 9 the transverse momentum distributions for the (^{11}Be,^{10} Be) reaction on silicon (upper panel) and on lead (lower panel) targets. One sees that the momentum distributions are somewhat distorted by the Coulomb field for a silicon target, while for a lead target the effect is huge and the outcome is completely dominated by Coulomb repulsion. The transverse momentum transfer to the core fragments after the stripping can be roughly estimated by the relation $\Delta P_c = Z_c Z_T e^2/bv$, where b is the impact parameter and v is the projectile velocity. For the reaction on a lead target, $b \simeq 10$ fm and $v \simeq 0.4\ c$, leading to $\Delta P_c \simeq 110$ MeV/c. This is indeed where the broad peak in the momentum distribution (lower panel of figure 9) is located.

Finally, we remind the reader that the present paper is an analysis of the stripping reaction, also called inelastic breakup. For experiments that only observe the core fragment, there is also an incoherent contribution from elastic breakup, which is given by the coherent sum of the contributions from diffraction dissociation and Coulomb dissociation. The latter becomes dominant for the reaction of ^{11}Be on a heavy target such as gold [3] and will lead to momentum distributions that, in principle, are different from those shown in fig. 9.

IV. CALCULATION OF THE DOUBLE-DIFFERENTIAL STRIPPING CROSS SECTION AND COMPARISONS WITH EXPERIMENT

A. Alignment of the reaction residues

Except for the special case in which the wave function factorizes in Cartesian coordinates, the longitudinal and transverse momentum components will be coupled. This is of primary importance for the analysis of experiments in which the detection system limits the accep-

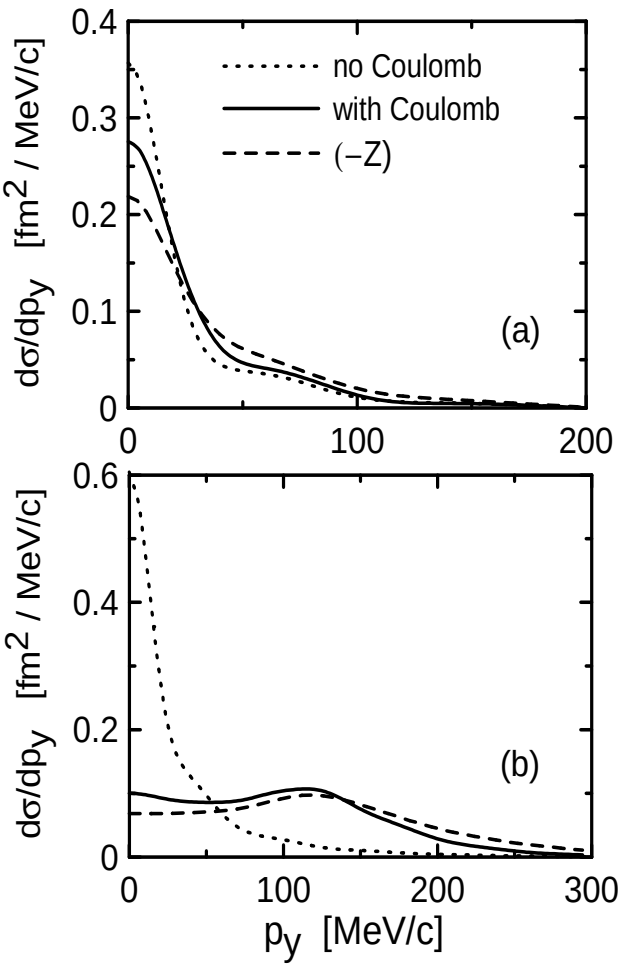

FIG. 9: Transverse momentum distributions of ^{10}Be fragments for the reaction (^{11}Be,^{10}Be) at 80 MeV/nucleon. The solid (dotted) curves include (do not include) the core-target Coulomb interaction. The upper panel (a) is for Si targets, while the lower panel (b) is for Pb targets. Changing the sign of the charge of the target yields the dashed curves.

tance of events to a certain volume in momentum space, a problem that until now has been treated in simple approximations. The selection in (P_z, $P_\perp$) space may also in special cases provide an additional spectroscopic tool. In order to illustrate the phenomenon, we plot in fig. 10 the double differential cross section $d^2\sigma/dP_z dP_\perp$ for the reaction of a deeply bound $l = 2$ state calculated from eq. (23). The momentum distributions for the $l = 0$ and the three $l = 2$ states are shown separately. For the case $l = 2$, the distributions for the three m states are peaked in different regions of the P_z-$P_\perp$ plane. The maps of fig. 10 are clearly necessary input to an accurate calculation of the experimental acceptance.

We have already pointed out that the reactions favor the formation of residues in states with the maximum absolute value of the magnetic quantum number $m = \pm l$ (with the quantization axis taken to be the beam direction). This (possible) alignment effect implies a (possible) anisotropic emission (in the center-of-mass system) of gamma rays emitted after the reaction. This is a tool for identifying multipolarities of the gamma transitions and spin sequences in the product nucleus. The fact that for different values of m, the main

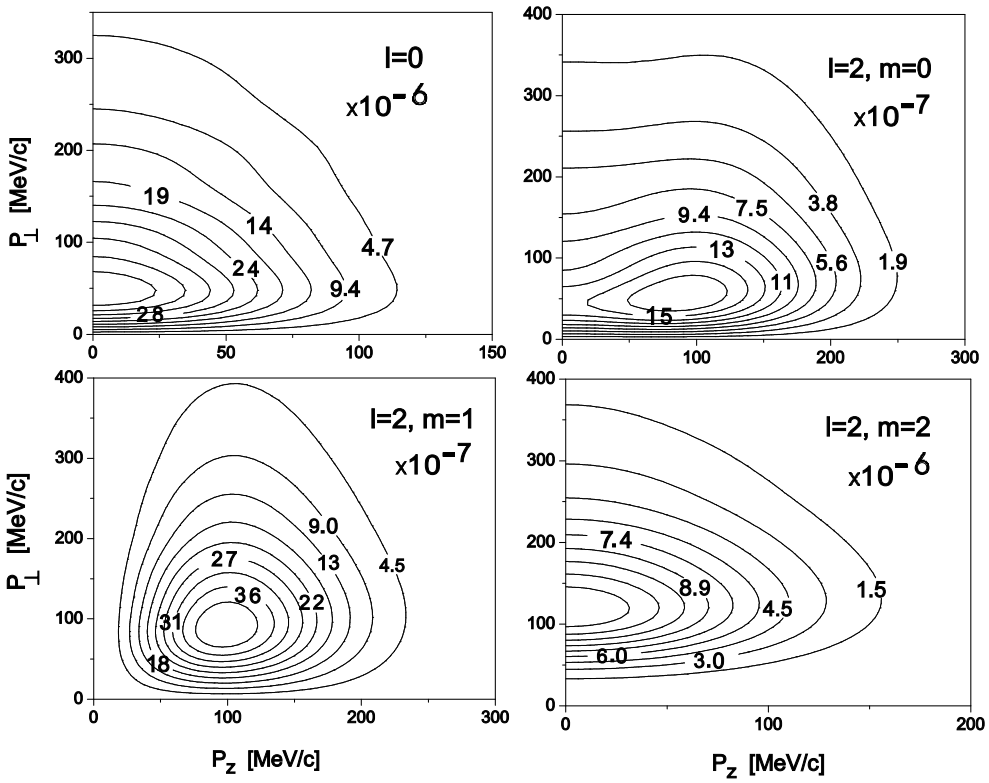

FIG. 10: Contour plots for the $l = 0, 2$ knockout reactions ^{9}Be (^{34}Ar,^{33} Ar) X at 68.2 MeV/nucleon. The contour lines are equidistant. The projections on one Cartesian coordinate axis were illustrated in figs. 4, 7, and 8. The absolute values of $d^2\sigma/dP_z dP_\perp$ (in fm^2/(MeV/c)^2) are given by the numbers in the contour plots, which are to be multiplied by the factors shown in each panel.

contributing cross sections are located in different areas of the (P_z, $P_\perp$) map suggests that the alignment effect can be enhanced by making cuts in the momentum components. A theoretical example of such an application has been given in fig. 12 of ref. [1], which shows the calculated angular distributions for two different spin sequences. For the example given in fig. 11, the $m = 2$ fraction in the reaction residues is ("set 1") 58% as compared with 40% for a population with statistical weights. Selecting reactions with P_z values between -50 and 50 MeV/c ("set 2") increases the $m = 2$ fraction to 85% and reduces the count rate to one half, corresponding to a net gain in sensitivity. Limiting in addition the values of $P_\perp$ to values between 85 and 165 MeV/c gives only a marginal improvement: The $m = 2$ fraction increases to 88% but at the cost of reducing the intensity by another factor of one half.

As an example of a possible application of the alignment effect, we show in fig. 11 angular distributions of gamma rays in the center-of-mass system calculated from the expressions given by Yamazaki [28]. The example is for an assumed $\frac{3}{2}^+$ to $\frac{1}{2}^+$ cascade as in ^{33}Ar and for various assumed multipoles and mixing ratios. The alignment parameters correspond to "set 2", which gives results that are already approaching pure $m = \pm 2$ alignment. Without the cut on P_z, the anisotropy would be only half as big.

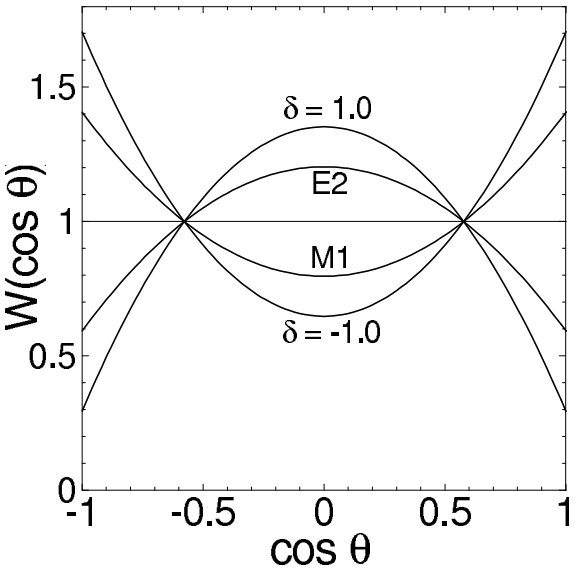

FIG. 11: Gamma-ray angular distributions for a $\frac{3}{2}^+$ to $\frac{1}{2}^+$ transition with alignment parameters corresponding to "set 2" (in the text) obtained by a central cut on the parallel momentum. Calculations are shown for the multipolarities E2, M1, and for mixed transitions with E2/M1 amplitudes of ± 1.0.

B. Comparisons with experiment

The present work deals with an extension of a theory [9, 10] that has been tested in numerous experiments. As indicated in subsect. III A the longitudinal momentum distributions are well in hand, both experimentally and theoretically. There is little reason to doubt that the same is the case for the transverse-momentum distributions calculated here. However, there are few good data sets to compare with. Most published transverse distributions are superpositions of contributions from several l values and would require gamma coincidence data to provide detailed test of the calculations. However, the proton knockout on ^{8}B is an exception to this.

For ^{8}B, the inclusive transverse-momentum distribution in the knockout of the halo proton has been measured in the experiment by Kelley *e*t al. [29]. In spite of the absence of gamma-ray coincidence data, this is a favorable case because the ground-state cross section dominates and because the approximately 15% branch to the excited level also has $l = 1$ and has an almost identical shape. Fig. 12 shows that our calculation is in excellent agreement with the data, which it reproduces over two orders of magnitude in cross section. There are several measurements of the longitudinal-momentum distribution for ^{8}B proton knockout; fig. 4 of ref. [1] presents a comparison of high-energy data with a black-disk calculation, essentially indistinguishable from fig. 3 of the present work.

Our second comparison with experimental data illustrates how the calculations in the present work may be applied toward clarifying a much more complicated issue. The reactions and structure of the two-neutron halo nucleus ^{11}Li have attracted much interest. It is a Borromean system in the sense that although the three-body system, consisting of ^{9}Li and two neutrons, forms a bound state, none of the possible two-body subsystems have bound states. Hence the stability of ^{11}Li is brought about by the interplay of the core-neutron and the neutron-neutron interactions, which must lead to a strongly correlated wave function with the two neutrons spatially close together. Barranco *et al.* [30] found

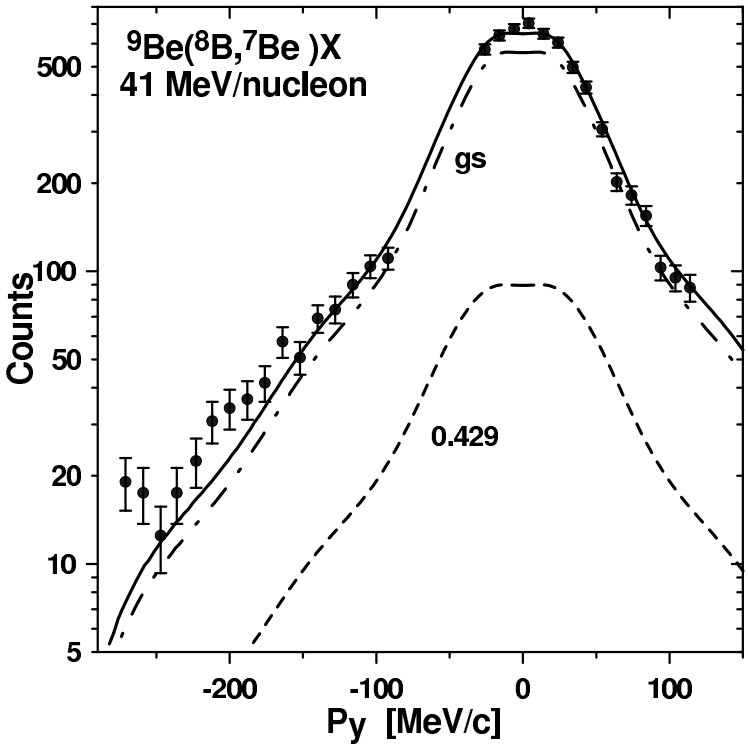

FIG. 12: Inclusive transverse-momentum distribution for the residue in the ^{9}Be(^{8}B,^{7}Be$_{gs}$)X reaction measured at 41 MeV/nucleon [29]. The theoretical calculation (full drawn) is based on the same parameter set as fig. 3, and the only adjustable parameter is the (arbitrary) scale. The binding energy for this proton halo state is 0.137 MeV. The dot-dashed and dashed curves are the individual contributions of the ^{7}Be ground state and first-excited state, respectively. The angular resolution in the experiment broadens the data by approximately 4%. This has not been included in the theoretical curves.

that attempts to understand ^{11}Li via breakup reactions are made difficult by important final-state interactions, so that the primary mechanism is removal of a single neutron followed by the decay in flight of the unstable ^{10}Li. The slow neutron emerging from this decay carries no direct information on the ^{11}Li structure; its energy spectrum reflects properties of both the initial and final state.

Simon *et al.* [31] showed that this problem can be circumvented by reconstructing the momentum vector of the ^{10}Li intermediate from the observed momenta of ^{9}Li and a neutron following a reaction on a carbon target. In an experiment at 287 MeV/nucleon they obtained the best resolution for the projected transverse-momentum component and arrived at the spectrum shown in fig. 13. The momentum resolution (full width at half maximum) was approximately 55 MeV/c [32]. Their analysis was based on a simplified model using analytical approximations to the momentum distributions and found the spectrum to require an $(1s_{1/2})^2$ component of (45±10)%, the rest being $(0p_{1/2})^2$. They obtained further confirmation of this interpretation by measuring the angular distribution of the neutron relative to a quantization axis taken along the recoil direction of the ^{10}Li composite. This distribution showed the forward-backward asymmetry characteristic of interference between final states of opposite parity.

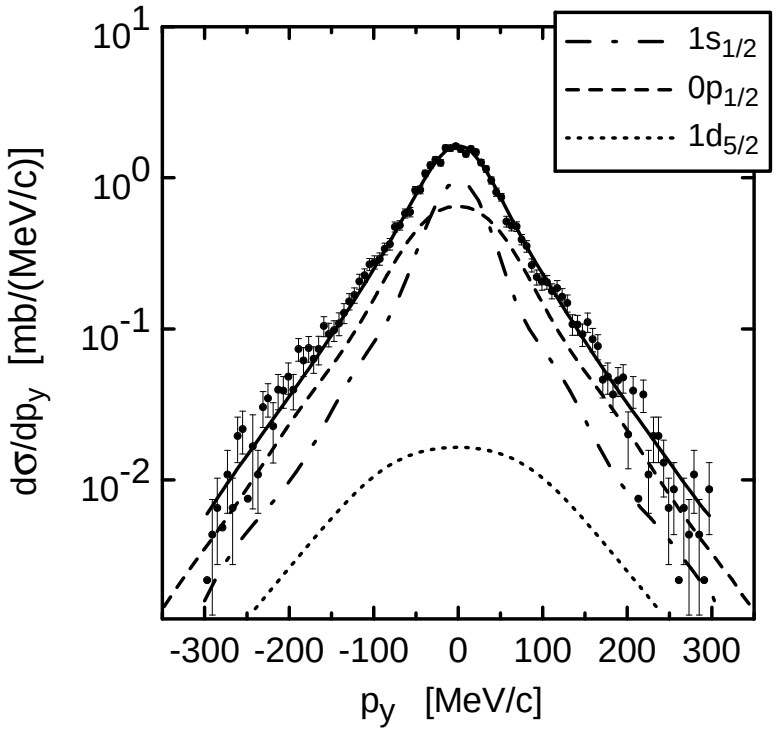

FIG. 13: Inclusive transverse-momentum distribution for the residue in the inclusive ^{12}C(^{11}Li,^{10}Li)X reaction measured at 287 MeV/nucleon [31]. The theoretical result (full drawn curve) is the adjusted sum of three angular-momentum components as described in the text.

For the calculation here we approximate the ^{11}Li ground state by an inert ^{9}Li core coupled to a neutron pair in a mixture of $(1s_{1/2})^2$, $(0p_{1/2})^2$, and $(0d_{5/2})^2$ states. We assume a two-body model, thus neglecting interference effects, and adjust the single-particle wave functions to reproduce the effective neutron separation energies. The two-neutron separation energy is 0.3 MeV and to this comes the average excitation energies of the three states in ^{10}Li. From the systematics in fig. 6 of [33] augmented with data for the $0d_{5/2}$ neutron states in neighboring nuclei we estimate ^{10}Li average excitation energies to 0.2, 0.5, and 1.5 MeV for the three single-particle states, respectively. In the spirit of the sudden approximation, we take these to be the center of gravity for the multiplets formed by the coupling to the ^{9}Li spin and arrive at effective neutron-separation energies of 0.5, 0.8, and 1.8 MeV, still in the same order, which determine the relative core-particle wave functions of the system ^{10}Li+n. The sudden approximation suggests that the same wave functions should be used for calculating the S matrices (profile functions) for ^{10}Li treating it as a neutron+^{9}Li composite as described in ref. [9]. The three spectroscopic factors are then obtained from an adjustment to the differential cross section as shown in fig. 13.

The calculated transverse-momentum distributions for the assumed three components were folded with the experimental resolution. The sum of the resulting distributions, weighted with the unknown spectroscopic factors, were adjusted in a χ^2 analysis to the experimental result as shown in fig. 13. Per degree of freedom, the goodness of the fit

is $\chi^2/\nu = 1.38$ for absolute spectroscopic factors of 0.98(6) ($1s_{1/2}$), 1.91(16) ($0p_{1/2}$), and 0.12(10) ($0d_{5/2}$). In view of the many approximations made in this analysis, it is probably satisfactory that the the sum of the spectroscopic factors is 3.0, where the sum-rule value is 2. Re-normalized to the sum, the relative contributions are 33(2)%, 64(5)%, and 4(3)% in approximate agreement with the analysis of Simon *et al.* [31] cited above, who obtained 45% for the $1s_{1/2}$ state. The errors cited do not include systematic contributions arising from the theory or contained in the experimental data. It is interesting to compare with the neighboring nucleus ^{12}Be [11], also with 8 neutrons, for which the $0d_{5/2}$ contribution to the one-neutron knockout reaction appears to be much larger, of the order of 50%.

V. CONCLUDING REMARKS

The present work has extended the theory of one-nucleon stripping reactions (inelastic breakup) to cover two-dimensional momentum distributions of the reaction residue with the use of realistic profile functions for the core-target and nucleon-target interactions. The parallel-momentum distributions, projections on the beam direction P_z, are not appreciably different from those obtained in the "black disk" approximation used in earlier work. On the other hand, the projections on the transverse direction, here referred to as P_y, are very different from the projections on P_z. For halo systems they show a weak component, which represents an additional mechanism in which the residue has scattered elastically on the target. For more strongly bound systems the two processes, stripping and elastic scattering, become inseparable, and the distributions on P_y are broader than those on P_z.

The doubly-differential distribution of the cross section on the parallel- and transverse-momentum variables (P_z,$P_\perp$) has for a given angular momentum $l \geq 1$ a characteristic behavior for the different components of the magnetic quantum number m. This will be of importance for evaluating acceptance corrections in experiments. The m dependence of the cross sections leads to alignment of the residues and consequently to anisotropic emission of subsequent gamma rays. This effect can be exploited for identifying spin sequences and gamma-ray multipolarities as illustrated in the example in fig. 11. A measurement of the transverse momentum distribution in stripping of ^{8}B on a light target is in excellent agreement with our calculation, which reproduces the experimental result accurately over two orders of magnitude in cross section. We have also attempted a more tenuous application of the theory to the complex case of neutron knockout on the two-neutron halo nucleus ^{11}Li.

VI. APPENDIX: GAUSSIAN EXPANSION METHOD FOR STRIPPING REACTIONS

Using the explicit form of the spherical harmonics

$$\begin{aligned} Y_{lm}\left(\widehat{\mathbf{r}}\right) &= (-1)^m \sqrt{\frac{2l+1}{4\pi}} \sqrt{\frac{(l-m)!}{(l+m)!}}\; P_{lm}\left(\cos\theta\right)\; e^{im\phi} \\ &= C_{lm} P_{lm}\left(\cos\theta\right)\; e^{im\phi} \end{aligned} \tag{25}$$

and

$$\mathbf{k}_c \cdot \mathbf{r} = k_\perp r \sin\theta \cos\left(\phi_k - \phi\right) + k_z r \cos\theta \ . \tag{26}$$

Part of the integral in (2) is

$$\begin{aligned}\mathcal{F}_{lm}\left(k_\perp, k_z, b_n\right) &= \int d^3r\ e^{-i\mathbf{k}_c\cdot\mathbf{r}} S_c\left(b_c\right)\psi_{lm}\left(\mathbf{r}\right) \\ &= C_{lm}\int dr\ r^2\ \sin\theta\ d\theta\ d\phi \\ &\times\ \exp\left\{-i\left[k_\perp r\sin\theta\cos\left(\phi_k-\phi\right)+k_z r\cos\theta\right]\right\} \\ &\times\ S_c\left(\sqrt{r^2\sin^2\theta+b_n^2-2r\sin\theta\ b_n\cos\left(\phi-\phi_n\right)}\right) \\ &\times\ R_l\left(r\right)\ P_{lm}\left(\cos\theta\right)\ e^{im\phi}\ . \end{aligned} \tag{27}$$

To simplify the calculations we can express $S_c\left(b_c\right)$ as an expansion in terms of integrable functions. The S-matrices can be well described by the expansion

$$S_c\left(b_c\right)=\sum_j^N \alpha_j\ \exp\left[-b_c^2/\beta_j^2\right]\ , \qquad \text{with} \quad \beta_j=\frac{R_L}{j}\ . \tag{28}$$

Good fits for realistic S-matrices were obtained with $N=20$, i.e. with 20 complex coefficients α_j and $R_L=10-20$ fm, depending on the size of the system. Since the real part of the S-matrices has the usual behavior of $S_c\left(b_c\right)\sim 0$ for $b_c \ll R$, and $S_c\left(b_c\right)\sim 1$ for $b_c \gg R$, where R is a generic nuclear size, one of the coefficients of the expansion in eq. (28) is $\alpha_j=1$, and $\beta_j=\infty$, which we take as the $j=0$ term in the expansion.

We now use the sum (28) and the equation

$$\exp\left(-iz\cos\phi\right)=\sum_{p=-\infty}^{\infty} i^p J_p\left(z\right)\ e^{ip\phi}\ , \tag{29}$$

valid for any complex z, in equation (27).

The integration in eq. (27) will then involve functions of the form

$$\begin{aligned}\mathcal{F}_{lm,\ j}\left(k_\perp, k_z, b_n\right) &= C_{lm}\ \alpha_j\int d\rho\ \rho\ dz\ d\phi \\ &\times\ R_l\left(r\right)\ P_{lm}\left(\cos\theta\right)\ \exp\left[-\left(\boldsymbol{\rho}-\mathbf{b}_n\right)^2/\beta_j^2\right] \\ &\times\ e^{im\phi}\ \exp\left\{-ik_\perp\rho\cos\left(\phi_k-\phi\right)\right\}\ \exp\left[-ik_z z\right]\ , \end{aligned} \tag{30}$$

where $\mathbf{r}\equiv(\boldsymbol{\rho}, z)$, $\cos\theta=z/r=z/\sqrt{\rho^2+z^2}$. Then

$$\begin{aligned}\mathcal{F}_{lm,\ j}\left(k_\perp, k_z, b_n\right) &= C_{lm}\ \alpha_j\ \exp\left[-b_n^2/\beta_j^2\right]\int d\rho\ \rho\ \exp\left[-\rho^2/\beta_j^2\right] \\ &\times\ \int dz\ \exp\left[-ik_z z\right]\ R_l\left(r\right)\ P_{lm}\left(\cos\theta\right) \\ &\times\ \int d\phi\ e^{im\phi}\ \exp\left\{-ik_\perp\rho\cos\left(\phi_k-\phi\right)\right\}\ \exp\left[\frac{2\rho b_n}{\beta_j^2}\cos\left(\phi-\phi_n\right)\right]\ . \end{aligned} \tag{31}$$

Using the expansion (29), we can write

$$\begin{aligned}&\exp\left\{-ik_\perp\rho\cos\left(\phi_k-\phi\right)\right\}\ \exp\left[\frac{2\rho b_n}{\beta_j^2}\cos\left(\phi-\phi_n\right)\right] \\ &= \sum_{p,\ p'} i^{p+p'} J_p\left(k_\perp\rho\right)\ J_{p'}\left(i\frac{2\rho b_n}{\beta_j^2}\right)\ \exp\left[ip\left(\phi_k-\phi\right)\right]\ \exp\left[ip'\left(\phi-\phi_n\right)\right]\ . \end{aligned} \tag{32}$$

Since

$$\int d\phi \; e^{im\phi} e^{-ip\phi} e^{ip'\phi} = 2\pi \delta_{m-p,\; p'} \; ,$$

then

$$\int d\phi \; e^{im\phi} \; \exp\left\{-ik_\perp \rho \cos\left(\phi_k - \phi\right)\right\} \; \exp\left[\frac{2\rho b_n}{\beta_j^2} \cos\left(\phi - \phi_n\right)\right] \tag{33}$$

$$= \; 2\pi i^m \exp\left[-im\phi_n\right] \sum_p J_p\left(k_\perp \rho\right) J_{m-p}\left(i\frac{2\rho b_n}{\beta_j^2}\right) \exp\left[ip\left(\phi_k + \phi_n\right)\right] \quad . \tag{34}$$

Thus

$$\begin{aligned} \mathcal{F}_{lm,\; j}\left(k_\perp, k_z, b_n\right) \; &= \; 2\pi \; C_{lm} \; i^m \; \alpha_j \; \exp\left[-im\phi_n\right] \; \exp\left[-b_n^2/\beta_j^2\right] \\ &\times \; \sum_p \exp\left[ip\left(\phi_k + \phi_n\right)\right] \\ &\times \; \int_0^\infty d\rho \; \rho \; J_p\left(k_\perp \rho\right) \; \exp\left[-\rho^2/\beta_j^2\right] \; J_{m-p}\left(i\frac{2\rho b_n}{\beta_j^2}\right) \\ &\times \; \int_{-\infty}^\infty dz \; \exp\left[-ik_z z\right] \; R_l\left(r\right) \; P_{lm}\left(\cos\theta\right) \; . \end{aligned} \tag{35}$$

Upon squaring eq. (35), inserting in eq. (2), and integrating over ϕ_k and ϕ_n, we can use $\int d\phi \; e^{ip\phi} e^{-ip'\phi} = 2\pi \delta_{p,\; p'}$ and we get

$$\frac{d\sigma_{\rm str}}{k_\perp dk_\perp dk_z} = \; \frac{2\pi}{2l+1} \int_0^\infty db_n \; b_n \; \left[1 - \left|S_n\left(b_n\right)\right|^2\right] \; \sum_{m,\; p} C_{lm}^2 \; \left|\mathcal{A}_{lmp}\left(k_\perp, k_z, b_n\right)\right|^2 , \tag{36}$$

where

$$\begin{aligned} \mathcal{A}_{lmp}\left(k_\perp, k_z, b_n\right) \; &= \; \sum_{j=0}^N \alpha_j \; \exp\left[-b_n^2/\beta_j^2\right] \\ &\times \; \int_0^\infty d\rho \; \rho \; J_p\left(k_\perp \rho\right) \exp\left[-\rho^2/\beta_j^2\right] \; J_{m-p}\left(i\frac{2\rho b_n}{\beta_j^2}\right) \\ &\times \; \int_{-\infty}^\infty dz \; \exp\left[-ik_z z\right] \; R_l\left(r\right) \; P_{lm}\left(\cos\theta\right) \; . \end{aligned} \tag{37}$$

Since

$$I_\alpha\left(x\right) = i^{-\alpha} J_\alpha\left(ix\right) ,$$

where $I_\alpha\left(x\right)$ is the modified Bessel function, one gets

$$\begin{aligned} \mathcal{A}_{lmp}\left(k_\perp, k_z, b_n\right) \; &= \; \sum_j \alpha_j \; \exp\left[-b_n^2/\beta_j^2\right] \\ &\times \; \int_0^\infty d\rho \; \rho \; J_p\left(k_\perp \rho\right) \exp\left[-\rho^2/\beta_j^2\right] \; I_{m-p}\left(\frac{2\rho b_n}{\beta_j^2}\right) \\ &\times \; \int_{-\infty}^\infty dz \; \exp\left[-ik_z z\right] \; R_l\left(r\right) \; P_{lm}\left(\cos\theta\right) \; , \end{aligned} \tag{38}$$

where an irrelevant phase i^{m-p} was dropped off, as only the absolute value of $\mathcal{A}_{lmp}$ enters eq. (36).

The first term of the equation (38), with $\beta_j = \infty$ and $\alpha_j = 1$ can be calculated using $I_\alpha(0) = \delta_\alpha$.

Using the integral

$$\int_0^\infty dk_\perp \; k_\perp \; J_p(k_\perp \rho) \; J_p(k_\perp \rho') = \frac{1}{\rho} \, \delta(\rho - \rho') \;\; , \tag{39}$$

in eq. (36) one gets for the *longitudinal momentum distribution*

$$\frac{d\sigma_{\rm str}}{dk_z} = \frac{2\pi}{2l+1} \int_0^\infty db_n \; b_n \; \left[1 - |S_n(b_n)|^2\right] \; \sum_{m,\; p} C_{lm}^2 \; \int_0^\infty d\rho \; \rho \; |\mathcal{B}_{lmp}(k_z, b_n, \rho)|^2 \, , \tag{40}$$

where

$$\begin{aligned} \mathcal{B}_{lmp}(k_z, b_n, \rho) \; &= \; \sum_j \alpha_j \; \exp\left[-b_n^2/\beta_j^2\right] \; \exp\left[-\rho^2/\beta_j^2\right] \\ &\times \; I_{m-p}\left(\frac{2\rho b_n}{\beta_j^2}\right) \int_{-\infty}^\infty dz \; \exp\left[-ik_z z\right] \; R_l(r) \; P_{lm}(\cos\theta) \;\; . \end{aligned} \tag{41}$$

Using the integral of eq. (6) in eq. (36) one gets for the *transverse momentum distribution*

$$\frac{d\sigma_{\rm str}}{d^2 k_\perp} = \frac{2\pi}{2l+1} \; \int_0^\infty db_n \; b_n \; \left[1 - |S_n(b_n)|^2\right] \; \sum_{m,\; p} C_{lm}^2 \; \int_{-\infty}^\infty dz \; |\mathcal{D}_{lmp}(k_\perp, b_n, z)|^2 \, , \tag{42}$$

where

$$\begin{aligned} \mathcal{D}_{lmp}(k_\perp, b_n, z) \; &= \; \sum_{j=0}^N \alpha_j \; \exp\left[-b_n^2/\beta_j^2\right] \\ &\times \; \int_0^\infty d\rho \; \rho \; J_p(k_\perp \rho) \exp\left[-\rho^2/\beta_j^2\right] \; I_{m-p}\left(\frac{2\rho b_n}{\beta_j^2}\right) R_l(r) \; P_{lm}(\cos\theta) \;\; . \end{aligned} \tag{43}$$

The formulas above are also useful to check the quality of the Gaussian fit, eq. (28), to obtain the momentum distributions. One can compare the direct numerical integrations using eq. (40) with

$$\begin{aligned} \frac{d\sigma_{\rm str}}{dk_z} \; &= \; \frac{1}{2l+1} \int_0^\infty db_n \; b_n \; \left[1 - |S_n(b_n)|^2\right] \; \sum_m \int_0^\infty d\rho \; \rho \; \int_0^{2\pi} d\phi \\ &\times \; \left| \int_{-\infty}^\infty dz \; \exp\left[-ik_z z\right] \; \psi_{lm}(\mathbf{r}) \right|^2 \; |S_c(b_c)|^2 \\ &= \; \frac{1}{2l+1} \int_0^\infty db_n \; b_n \; \left[1 - |S_n(b_n)|^2\right] \; \sum_m C_{lm}^2 \; \int_0^\infty d\rho \; \rho \\ &\times \; |\mathcal{Z}_{lm}(k_z, \rho)|^2 \; \mathcal{S}(b_n, \rho) \, , \end{aligned} \tag{44}$$

where

$$\begin{aligned} \mathcal{Z}_{lm}(k_z, \rho) \; &= \; \int_{-\infty}^\infty dz \; \exp\left[-ik_z z\right] \; R_l(r) \; P_{lm}(\cos\theta) \\ \mathcal{S}(b_n, \rho) \; &= \; \int_0^{2\pi} d\phi \; \left| S_c\left(\sqrt{\rho^2 + b_n^2 - 2\rho \; b_n \cos\phi}\right) \right|^2 , \end{aligned} \tag{45}$$

which is the same as eq. (5).

Acknowledgments

We have benefited from comments by Henning Esbensen, Kai Hencken and Jeffrey A. Tostevin. This work was supported by the National Science Foundation under Grants No. PHY-0110253 and PHY-0070911.

---

[1] P. G. Hansen and J. A. Tostevin, Annu. Rev. Nucl. Part. Sci. **53**, 219 (2003).
[2] C. A. Bertulani and K. W. McVoy, Phys. Rev. C **46**, 2638 (1992).
[3] R. Anne *et al.*, Nucl. Phys. A **575**, 125 (1994).
[4] P. G. Hansen, A. S. Jensen and B. Jonson, Annu. Rev. Nucl. Part. Sci. **45**, 505 (1995).
[5] P. G. Hansen, Phys. Rev. Lett. **77**, 1016 (1996).
[6] H. Esbensen, Phys. Rev. C **53**, 2007 (1996).
[7] K. Hencken, G. Bertsch and H. Esbensen, Phys. Rev. C **54** (1996) 3043.
[8] A. Navin *et al.*, Phys. Rev. Lett. **81**, 5089 (1998).
[9] J. A. Tostevin, J. Phys. G **25**, 735 (1999).
[10] J. A. Tostevin, Nucl. Phys. A **682**, 320c (2001).
[11] A. Navin *et al.*, Phys. Rev. Lett. **85**, 266 (2000).
[12] T. Aumann *et al.*, Phys. Rev. Lett. **84**, 35 (2000).
[13] V. Maddalena *et al.*, Phys. Rev. C **63**, 024613 (2001).
[14] J. Enders *et al.*, Phys. Rev. C **67**, 064301 (2003).
[15] J. S. Al-Khalili, J. A. Tostevin and I. J. Thompson, Phys. Rev. C **54**, 1843 (1996).
[16] J. A. Tostevin and J. S. Al-Khalili, Nucl. Phys. A **616**, 418c (1997).
[17] C.A. Bertulani and P. Danielewicz, *Introduction to Nuclear Reactions* (IOP Publishing, Bristol, UK, 2004), chapter 8.
[18] L. Ray, Phys. Rev. C **20**, 1857 (1979).
[19] J. R. Terry *et al.*, Phys. Rev. C **69**, 054306 (2004).
[20] A. Gade *et al.*, Phys. Rev. Lett. (in press) (2004).
[21] R. Serber, Phys. Rev. **72**, 1008 (1947).
[22] R. Serber, Annu. Rev. Nucl. Part. Sci. **44**, 1 (1994).
[23] T. Kobayashi *et al.*, Phys. Rev. Lett. **60**, 2599 (1988).
[24] N. Orr *et al.*, Phys. Rev. Lett. **69**, 2050 (1992).
[25] A. Gade *et al.*, Phys. Rev. C **69**, 034311 (2004).
[26] J. A. Tostevin *et al.*, Phys. Rev. C **66**, 024607 (2002).
[27] H. Esbensen and G. F. Bertsch, Phys. Rev. C **66**, 044609 (2002).
[28] T. Yamazaki, Nuclear Data **A3**, 1 (1967).
[29] J. H. Kelley *et al.*, Phys. Rev. Lett. **77**, 5020 (1967).
[30] F. Barranco, E. Vigezzi and R. A. Broglia, Phys. Lett. B **319**, 387 (1993).
[31] H. Simon *et al.*, Phys. Rev. Lett. **83**, 496 (1999).
[32] H. Simon, private communication.
[33] P. G. Hansen, Nucl. Phys. A **682**, 310c (2001).
[34] W.H. Press, B.P. Flannery, S.A. Teukolsky, and W.T. Vetterling, *Numerical Recipes: The Art of Scientific Computing*, Cambridge University Press, New York, 1996.